A combined experimental and theoretical study of Rashba-split surface states on the $(\sqrt{3} \times \sqrt{3})$ Pb/Ag(111)$R30°$ surface

2014 New J. Phys. 16 045017

(http://iopscience.iop.org/1367-2630/16/4/045017)

New Journal of Physics
The open access journal at the forefront of physics
Deutsche Physikalische Gesellschaft DPG | IOP Institute of Physics

A combined experimental and theoretical study of Rashba-split surface states on the ($\sqrt{3} \times \sqrt{3}$) Pb/Ag (111)*R*30° surface

L El-Kareh[1], G Bihlmayer[2], A Buchter[3], H Bentmann[3,4], S Blügel[2], F Reinert[3,4] and M Bode[1]

[1] Physikalisches Institut, Experimentelle Physik II, Universität Würzburg, Am Hubland, D-97074 Würzburg, Germany
[2] Peter Grünberg Institut and Institute of Advanced Simulation, Forschungszentrum Jülich and JARA, D-52425 Jülich, Germany
[3] Physikalisches Institut, Experimentelle Physik VII, Universität Würzburg, Am Hubland, D-97074 Würzburg, Germany
[4] Karlsruhe Institute of Technology KIT, Gemeinschaftslabor für Nanoanalytik, D-76021 Karlsruhe, Germany
E-mail: lydia.el-kareh@physik.uni-wuerzburg.de

Received 29 November 2013, revised 3 February 2014
Accepted for publication 17 February 2014
Published 22 April 2014

New Journal of Physics **16** (2014) 045017

doi:10.1088/1367-2630/16/4/045017

Abstract

We report on a combined low-temperature scanning tunneling spectroscopy (STS), angle-resolved photoemission spectroscopy (ARPES), and density functional theory (DFT) investigation of the ($\sqrt{3} \times \sqrt{3}$)*R*30°Pb/Ag(111) surface alloy which provides a giant Rashba-type spin splitting. With STS we observed spectroscopic features that are assigned to two hole-like Rashba-split bands in the unoccupied energy range. By means of STS and quantum interference mapping we determine the band onsets, splitting strengths, and dispersions for both bands. The unambiguous assignment of scattering vectors is achieved by comparison to ARPES measurements. While intra-band scattering is found for both Rashba bands, inter-band scattering is only observed in the occupied energy range. Spin- and orbitally-resolved band structures were obtained by DFT calculations. Considering the scattering between states of different spin- and orbital character, the apparent deviation between

experimentally observed scattering events and the theoretically predicted spin polarization could be resolved.

Keywords: Rashba effect, spin–orbit coupling, scanning tunneling microscopy, angle resolved photo emission spectroscopy, density functional theory

1. Introduction

It is well known that the degeneracy of electronic states can be lifted by breaking the inversion symmetry of crystal lattices intrinsically (e.g. Dresselhaus effect) [1] or by introducing surfaces or interfaces (Rashba–Bychkov effect) [2]. For a Rashba-split two-dimensional electron gas spin degeneracy is lifted and the dispersion can be written as $E_{\uparrow,\downarrow}(k) = E_0 + \frac{\hbar^2}{2m^*}(k \pm k_0)^2$ where m^* is the effective mass and $2k_0$ is the momentum splitting. The energy splitting between the band onset and the crossing of the two inner branches at $k = 0$ is called the Rashba energy $\Delta E_R = \frac{\hbar^2 k_0^2}{2\,m^*}$. The first successful observation of a Rashba-split surface state was reported by La Shell *et al* [3] for Au(111), which exhibits a Rashba energy $\Delta E_R = 2.1$ meV only. Recently, so-called giant splittings have been found for $(\sqrt{3} \times \sqrt{3})$ surface alloys of heavy post-transition metals with noble metal fcc(111) surfaces [4–18]. In these systems the splitting can reach $\Delta E_R \approx 200$ meV.

In particular, the electronic structure of the $(\sqrt{3} \times \sqrt{3})$ Bi/Ag(111)$R30°$ surface has been studied intensively [5–7, 9, 14–17]. This surface alloy features two downwards dispersing surface states within the L-projected bulk band gap, an occupied s, p_z-like band and an (mostly) unoccupied p_x, p_y-derived band [7]. The band structure has been observed by angle-resolved photo emission spectroscopy (ARPES) [5, 6, 9, 16], scanning tunneling spectroscopy (STS) [5], and quasi-particle inference mapping (QPI) [15, 17]. These experimental results consistently show that the two surface state bands hybridize below the Fermi level [16, 17]. This hybridization goes along with a rather complex spin-polarization pattern, which was theoretically predicted by density functional theory (DFT) [7] and experimentally verified by spin-resolved ARPES [9] and QPI [17]. QPI maps observed by tunneling into empty sample states, however, were interpreted as evidence for conventional Rashba behavior in the p_x, p_y-derived band [15, 17], in apparent disagreement to theoretical results [7].

In contrast, the $(\sqrt{3} \times \sqrt{3})$ Pb/Ag(111) surface, which structurally forms the same alloy as Bi/Ag(111) [19], has been studied to a far lesser extent. Since lead (Pb) has one p electron less than bismuth, the bands shift upwards with respect to the Fermi level. Indeed, DFT calculations predict two spin-split states above the Fermi level [7]. As a result the bands relevant for the surface Rashba effect are mostly unoccupied and thereby largely unaccessible by ARPES [4, 5, 9, 20].

The theoretically determined positions of these Rashba states was found to critically depend on the vertical relaxation of the Pb atoms relative to the Ag atoms, Δ_z (see figure 1(a)). Two distinct scenarios have been considered in the DFT calculations of [7], as schematically represented in figures 1(b) and (c). In the first case at the self-consistent relaxation value of $\Delta_z = 0.97$Å (figure 1(b)), the band dispersion qualitatively resembles the dispersion of Bi/Ag (111) with a hybridization of both bands close to the onset of the lower Rashba band at about

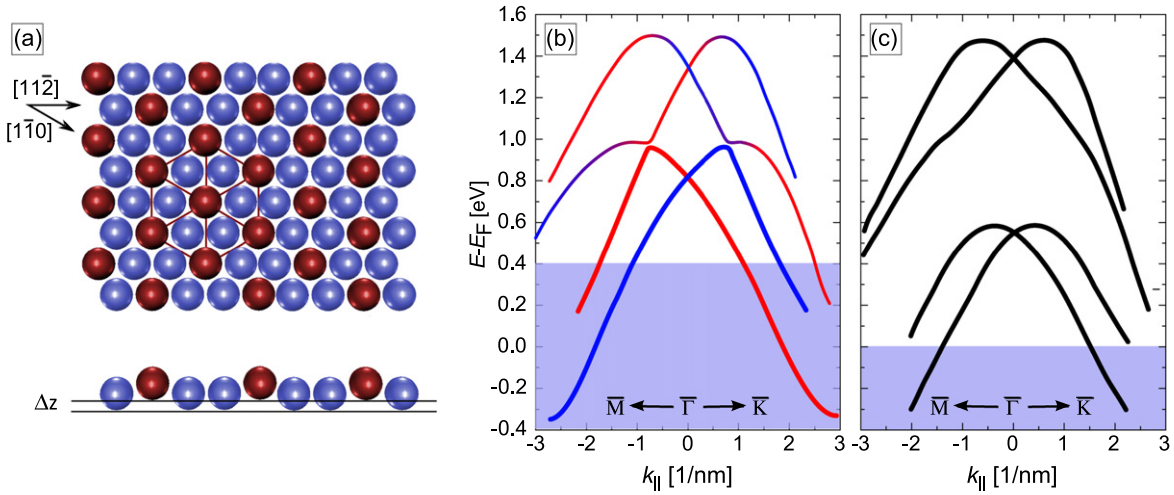

Figure 1. (a) Top and side view of the $(\sqrt{3} \times \sqrt{3})$ Pb/Ag$R30°$ structure with surface relaxation Δz of the Pb atoms. Pb atoms are red, Ag atoms blue. Schematics of the calculated dispersion of $(\sqrt{3} \times \sqrt{3})Pb/AgR30°$ for lead relaxation for surface relaxation values of (b) $\Delta_z = 0.97$ Å and (c) $\Delta_z = 0.67$Å (adapted from [7]). In (b) a hybridization between both surface states takes place. Red and blue represents the in-plane spin polarization. For smaller relaxation the lower (s, p_z-derived) Rashba band is shifting downwards (c), thereby increasing the energy separation between the two bands. See text for details.

1 eV above the Fermi level. However, this band position disagrees with ARPES measurements [4], which finds an extrapolated binding onset which differs by ≈ 400 meV from the DFT result. This offset is indicated by the blue shaded area in figure 1(b).

In order to improve the agreement between the experimentally observed band positions and the calculated surface electronic structure the relaxation value was tuned to $\Delta_z = 0.67$Å [7]. The resulting band structure is shown in figure 1(c). It agrees well with ARPES data [4] and the characteristically shaped van-Hove-like singularity which appears in STS spectra at 654 meV above the Fermi level [5].

Obviously, the smaller relaxation of the Pb atoms results in a larger inter-band spacing and the absence of any hybridization between the upper and the lower band. Since both models result in a very similar dispersion below the Fermi level, it is virtually impossible to verify one of the two models by ARPES measurements. In the case of figure 1(b) the branches observed below E_F would belong to two different surface states with a strong spin splitting, in the case of figure 1(c) both branches would originate from the same Rashba-split surface state with a smaller splitting. Experimentally even smaller outward relaxations of $\Delta_z = (0.46 \pm 0.06)$Å have been reported [21], pointing towards the model presented in figure 1(c).

In this report we study the $(\sqrt{3} \times \sqrt{3})$ Pb/Ag $R30°$ surface to solve some of the remaining questions. By means of scanning tunneling microscopy and derived spectroscopic methods we obtain insight into the electronic structure of occupied and empty states. Our STS results show two asymmetric peaks which are the fingerprints of the DOS of two Rashba-split surface states [5]. With this finding we can confirm the second predicted Rashba state and thus solve the unclear band onset situation in the unoccupied energy range. In the second step we used QPI mapping to observe spatial oscillations which originate from coherent elastic scattering between

two momentum eigenstates. By comparison with ARPES data the obtained energy dispersion and anisotropies of QPI are correlated to intra- or inter-band scattering vectors between specific bands. We extract effective masses and show that hexagonal warping exists for both bands. These experimental data are compared to DFT calculations of the $(\sqrt{3} \times \sqrt{3})Pb/AgR30°$ system. An excellent agreement, especially regarding the binding energy of the s, p_z-orbitals which was chronically overestimated so far, is found for a reduced outward relaxation of the Pb atom ($\Delta_z = 0.67$ Å). It is found that the scattering pattern observed in QPI can only be explained if—beyond the spin angular momentum—also the orbital momentum of the involved electronic states is considered.

2. Experimental details

2.1. STM setup

The STM experiments have been performed in a two-chamber UHV system equipped with a low-temperature STM working at 5 K. The system consists of separate chambers for sample preparation and surface analysis (base pressure $p \leqslant 1 \times 10^{-10}$ mbar). STM tips were electrochemically etched from a polycrystalline tungsten wire. The Ag(111) single-crystalline substrate was cleaned by cycles of Ar^+-sputtering ($E = 500$ eV) and subsequent annealing ($T \approx 700$ K). For preparation of the $(\sqrt{3} \times \sqrt{3})$Pb/Ag(111)$R30°$ surface alloy a third of a Pb monolayer was evaporated from a home-built Knudsen cell onto the Ag(111) substrate held at $T \approx 520$ K. STS spectra and dI/dU maps for QPI measurements have been taken by means of lock-in technique ($\nu = 789$ kHz).

2.2. ARPES setup

The ARPES data were collected with a hemispherical electron analyzer (Scienta R4000) and a monochromated He discharge lamp (MB Scientific) operating at an excitation energy of 21.22 eV (He Iα). The energy and angular resolutions were 7 meV and 0.3°, respectively. ARPES measurements were performed at a base pressure $p < 2 \times 10^{-10}$ mbar and a temperature of 25 K. The single-crystalline Ag(111) substrate was prepared by Ar^+-sputtering ($E = 500$ eV) and annealing ($T \approx 900$ K). Pb was evaporated from a commercial Knudsen cell at a rate of approximately 0.03 ML min^{-1}. Before each evaporation procedure the Ag(111) substrate was mildly annealed and subsequently allowed to cool down during evaporation. The formation of the surface alloy was confirmed by LEED.

2.3. DFT

The calculation of the surface electronic structure is based on DFT employing the full-potential linearized augmented plane-wave method as implemented in the FLEUR code[5]. The surface was simulated in a thin film geometry with a nine-layer Ag(111) film terminated on one end by the $(\sqrt{3} \times \sqrt{3})$ Pb/Ag(111)$R30°$ surface alloy reconstruction. For further specifications of the calculation, we refer the reader to [7, 13].

[5] For program description see http://www.flapw.de

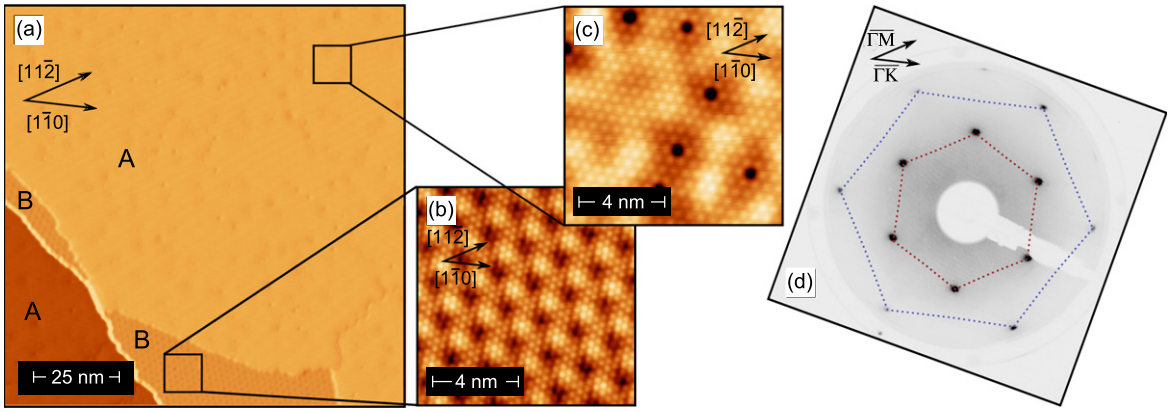

Figure 2. (a) Topography of Pb/Ag(111) at a Pb coverage just above one third of a monolayer (tunneling parameters: $I = 1$ nA, $U = 1.1$ V). Coexisting domains of the $(\sqrt{3} \times \sqrt{3})$ Pb/Ag(111)$R30°$ surface alloy (A) and the Pb wetting layer (B) can be recognized, which are shown atomically resolved in (b) and (c), respectively ((b) $I = 0.9$ nA, $U = 280$ mV; (c) $I = 300$ nA, $U = 50$ mV). Panel (d) shows the LEED pattern of the $(\sqrt{3} \times \sqrt{3})$ Pb/Ag(111)$R30°$ at $E = 55$ eV.

3. Results and discussion

3.1. Experimental results: STM and ARPES

Figure 2(a) shows the sample surface of Pb/Ag(111) at a Pb coverage just above one third of a monolayer. Coexisting domains of the $(\sqrt{3} \times \sqrt{3})$ Pb/Ag(111)$R30°$ surface alloy (A) and the Pb wetting layer (B) can be found on the surface [22]. The wetting layer domains shows a characteristic moiré pattern which can also be recognized in the atomically resolved STM image of figure 2(b). It is preferentially found at step edges. Figure 2(c) shows an atomically resolved image of the $(\sqrt{3} \times \sqrt{3})$ Pb/Ag(111)$R30°$ surface alloy with a few defects. The visible modulation originates from QPI and will be discussed in more detail below. figure 2(d) displays the corresponding LEED pattern. It consists of an outer hexagon that belongs to the underlying Ag(111) substrate and an inner hexagon which is rotated by 30° and reflects the $(\sqrt{3} \times \sqrt{3})$ $R30°$ symmetry of the surface alloy. figure 3 shows an averaged tunneling spectrum of the $(\sqrt{3} \times \sqrt{3})$ Pb/Ag(111)$R30°$ surface alloy. We can recognize two asymmetric peaks, the shape of which closely resembles the singularities described in [5]. The DOS of downwards dispersing Rashba-split bands is described by

$$\rho(E) = \begin{cases} \dfrac{|m^*|}{\pi\hbar^2}\sqrt{\dfrac{E_R}{E_0 - E}}, & E_0 - E_R < E < E_0 \\ \dfrac{|m^*|}{\pi\hbar^2} = \text{const}, & E < E_0 - E_R \\ 0, & \text{else} \end{cases} \tag{1}$$

where m^* is the effective mass. The Rashba energy $E_R = \frac{\hbar^2 k_0^2}{2\,m^*}$ describes the splitting strength. We have fitted the peaks following the algorithm described in [5]. Obviously, both peaks are

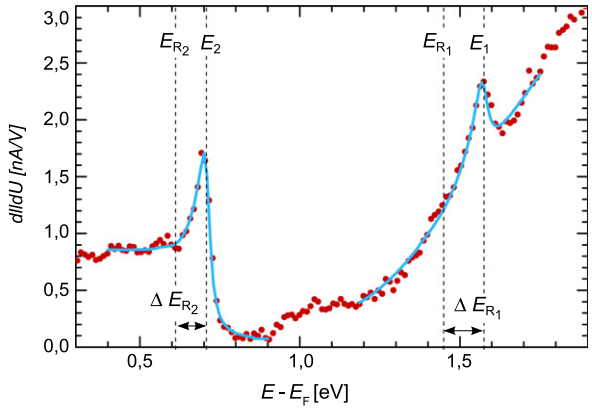

Figure 3. Tunneling spectrum (red dots) of the $(\sqrt{3} \times \sqrt{3})$ Pb/Ag(111)$R30°$ surface alloy showing two peaks at $E_1 = 1580$ meV and $E_2 = 710$ meV (set point: $I_{set} = 1$ nA, $U_{set} = -1$ V). The blue lines represent fits to the peaks (see text for details).

very well described by the fits and can clearly be assigned to the s, p_z- and the p_x, p_y-derived Rashba states as schematically represented in figure 1(c) ($\Delta_z = 0.67$) and described in [7]. For the p_x, p_y-derived state our fit results in $E_1 = (1580 \pm 5)$ meV and $\Delta E_{R_1} = (130 \pm 10)$ meV. For the s, p_z- derived band we obtain $E_2 = (710 \pm 5)$ meV and $\Delta E_{R_2} = (80 \pm 10)$ meV, i.e. slightly further away from the Fermi level than reported previously [5].

We would like to emphasize that in contrast to Bi/Ag(111), where we observed an obvious difference between the measured data and the fit for the occupied surface state due to a distinct shoulder [17], the agreement of the fit is very good for on Pb/Ag(111) at both peak positions. As has been pointed out in [17] the shoulder is ascribed to the opening of a hybridization gap which —as a result of the flat energy dispersion around the gap—leads to an enhanced DOS. Based on these observations we do not find any hint for hybridization of the two Rashba-split surface states on Pb/Ag(111), thereby favoring the model of figure 1(c).

To obtain the energy dispersion we measured two series of QPI maps by recording the spatial variation of the dI/dU signal in the bias range between −600 meV (occupied states) and 1600 meV (empty states) with an increment of 50 meV. Figure 4(a) shows the topography of the first sample area. Arrows indicate the crystallographic directions relative to the Pb overlayer, which are rotated by 30° with respect to the Ag(111) substrate, i.e. $\overline{\Gamma \mathrm{K}}_{\mathrm{Pb}} \| \overline{\Gamma \mathrm{M}}_{\mathrm{Ag}}$ and $\overline{\Gamma \mathrm{M}}_{\mathrm{Pb}} \| \overline{\Gamma \mathrm{K}}_{\mathrm{Ag}}$. We can recognize atomically flat terraces which are separated by two step edges oriented along different crystallographic directions. Again, at the step edges we can identify small domains of the Pb wetting layer on Ag(111). Figures 4(b) and (c) show the interference patterns measured at this location at $U = -163$ mV and $U = -263$ mV, respectively. Standing waves parallel to step edges and around defects are clearly visible. The corresponding FT QPI maps are shown in the insets. One can recognize a hexagonally shaped frame with cusps pointing into $\overline{\Gamma \mathrm{K}}$ directions. Close inspection of the inset figure 4(c) reveals a second hexagon which is slightly larger and much less pronounced. The latter hexagon is rotated by 30° with respect to the former, consequently pointing into $\overline{\Gamma \mathrm{M}}$ directions. The QPI maps for determining the electronic properties of the p_x, p_y-derived state have been measured on the same sample but at a different, second area, due to a tip change. The data obtained at the two positions have some

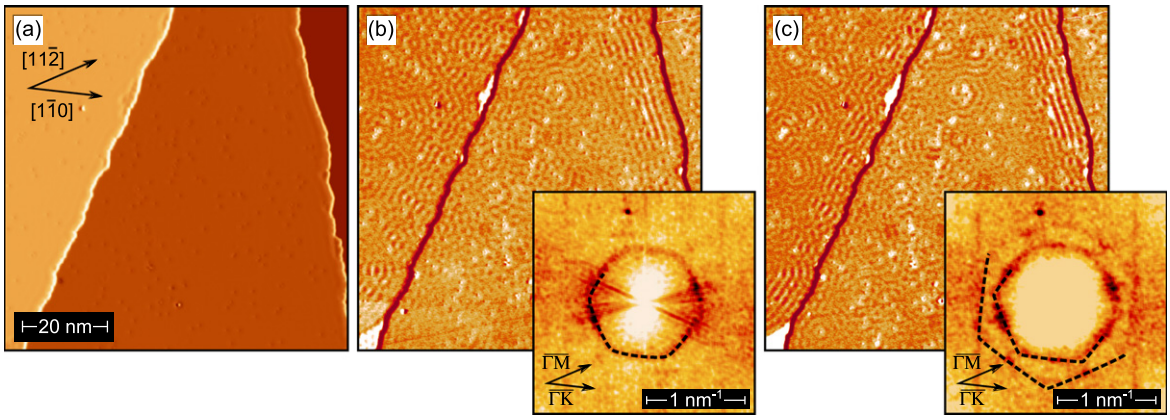

Figure 4. (a) Constant-current image of the $(\sqrt{3} \times \sqrt{3})$ Pb/Ag(111)$R30°$ surface alloy. (b) dI/dU map measured at $U = -163$ mV and (c) at $U = -263$mV. The insets show the corresponding Fourier-transformed (FT) dI/dU maps. The hexagonal shape of the FT depicts the anisotropic dispersion along the $\overline{\Gamma K}$ and $\overline{\Gamma M}$ directions.

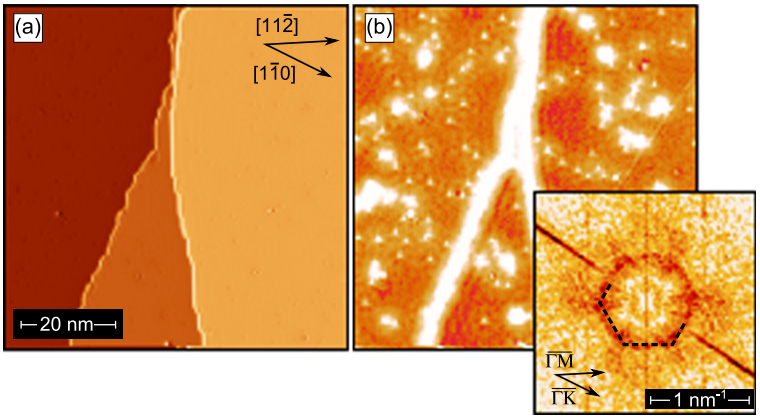

Figure 5. (a) Constant-current image of the $(\sqrt{3} \times \sqrt{3})$Pb/Ag(111)$R30°$ surface alloy. (b) dI/dU map measured at $U = 1037$ mV. The inset shows the corresponding two-dimensional Fourier-transformation of (b).

energetic overlap confirming compliance of the observed wave vectors. The constant-current STM topograph of this area is shown in figure 5(a). Again, one can recognize atomically flat terraces which are separated by two step edges. The pattern observed in figure 5(b) is not as strong and pronounced as the interference patterns in figures 4(b) or (c). We speculate that the weaker interference pattern is due to the reduced lifetime of electronic states which are energetically further away from the Fermi level. As we discuss later, there are different scattering processes responsible for the two energy regions. This might also affect the appearance of the patterns. In the corresponding 2D FFT (inset of figure 5(b)) we again observe a hexagonally shaped frame with cusps pointing into the $\overline{\Gamma M}$ directions.

The detailed analysis of the quasiparticle interference maps recorded over a wide range of bias voltages results in the extracted scattering vector $q(E)$ displayed in figure 6(a). Clearly, we observe an energy dispersion of $q(E)$ for both Rashba bands. Scattering within the p_x, p_y-derived

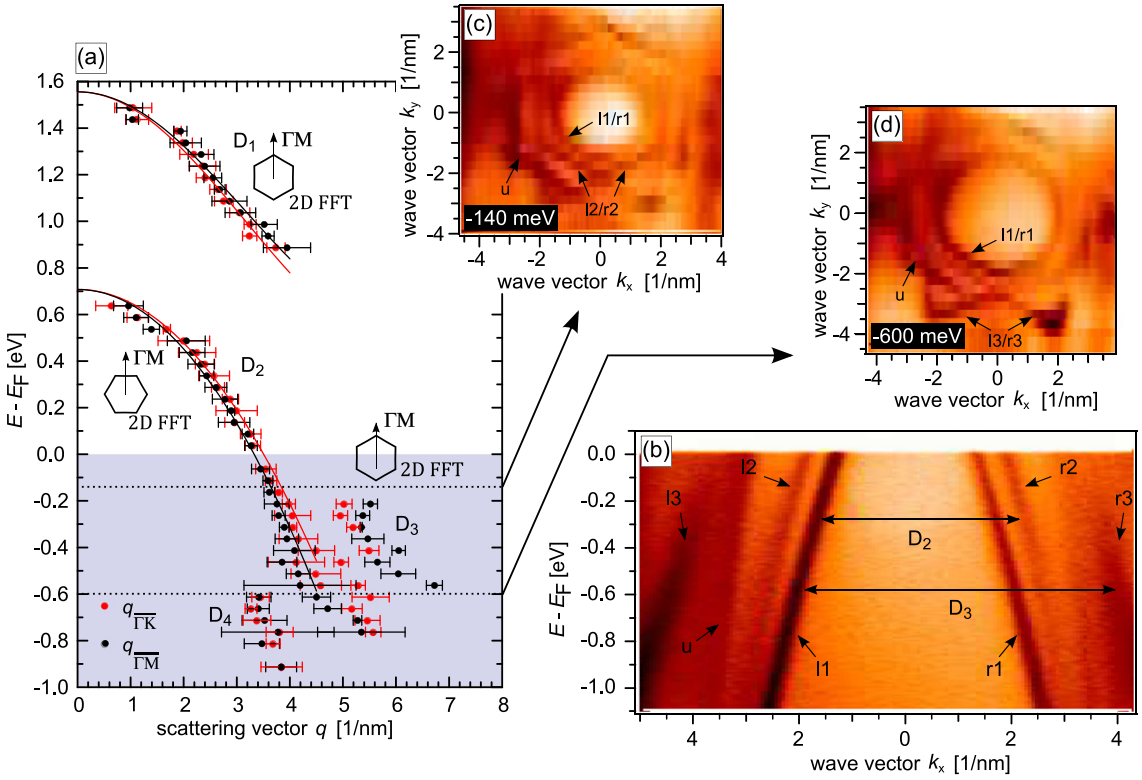

Figure 6. (a) Dispersion of scattering vectors q as extracted from two series of QPI maps shown in figures 4 and 5. Data measured along the $\overline{\Gamma K}$ and $\overline{\Gamma M}$ directions are plotted in red and black, respectively. Respective lines are the results of fits of intra-band scattering events. (b) Electronic structure of $(\sqrt{3} \times \sqrt{3})$ Pb/Ag(111)$R30°$ as determined by ARPES. The measured band structure along $\overline{\Gamma M}$ consists of three surface bands labeled by r1-r3 (l1-l3) at positive (negative) wave vectors and a bulk band u. Panels (c) and (d) show constant energy cuts of the band structure at two different energies as a function of both wave vector components k_x ($\overline{\Gamma M}$) and k_y ($\overline{\Gamma K}$).

band (labeled D_1 in figure 6) starts at about 1500 meV. The parabolic evolution of scattering vectors confirms the dominant role of intra-band scattering in this energy range ($q = 2k$ in this case). The dispersion was fitted with a cosine since it yields the best agreement to the experimentally observed scattering vectors. From this fit we obtain the band onset of the p_x, p_y-derived state at $E_1 = (1556 \pm 44)$ meV. This value is in good agreement with our STS data presented in figure 3, thereby confirming the model given in figure 1(c). We obtain effective masses of $m^*_{\overline{\Gamma K}} = (-0.14 \pm 0.01)m_e$ and $m^*_{\overline{\Gamma M}} = (-0.15 \pm 0.001)m_e$ along the two high-symmetry directions.

The analysis of the QPI maps taken in the energy range of the s, p_z-derived bands turned out to be not as straightforward. Surprisingly, we observe two and at some bias voltages even three scattering vectors, which are marked D_2, D_3 and D_4 in figure 6(a). The shorter scattering vector D_2 corresponds well to intra-band scattering events within the s, p_z-branches. Fitting D_2 with a parabolic function leads to $E_2 = (708 \pm 22)$ meV, which is in a good agreement with our STS data presented in figure 3. For the effective masses we obtain $m^*_{\overline{\Gamma K}} = (-0.166 \pm 0.005)m_e$

and $m^*_{\overline{\Gamma M}} = (-0.149 \pm 0.004) m_e$. These values are slightly different from data obtained in [5]. The signal D_3 in the coexistence area (labeled D_3 in figure 6(a)) shows the same anisotropy as the scattering events for the p_x, p_y-derived state.

In order to compare the scattering vectors D_2–D_4 obtained from QPI mapping with the occupied electronic band structure of Pb/Ag(111) we have performed ARPES measurements. The ARPES data are shown in figures 6(b)–(d). The spectrum in figure 6(b) shows the band dispersion along the $\overline{\Gamma M}$ direction. In agreement with previous works [4, 9] we identify three surface bands with negative effective mass m^* which are labeled accordingly (we follow the notation of [9]). In addition we observe the bulk band u that is back-folded due to the surface reconstruction [4]. The two inner bands originate from one Rashba-split surface band of mainly s, p_z orbital character with a momentum splitting of $2k_0 = 0.06(1)$ Å^{-1}. The momentum separation between r1 and l2 and the corresponding r2 and l1 branches indeed matches with the scattering vectors D_2 determined by STM. The outer branches r3 and l3 correspond to another surface band of p_x, p_y character. For this band the ARPES data do not allow us to deduce a finite momentum splitting. Within the measured energy window the splitting $2k_0$ of the p_x, p_y-band is smaller than ∼0.04 Å^{-1} and thus considerably reduced compared to the s, p_z-band. This finding is in line with DFT calculations presented below that indicate only a very small splitting of the p_x, p_y-band below E_F. The scattering vectors labelled D_3 can then be assigned to scattering events between the bands l3 and r1 or between the corresponding bands r1 and l3. The origin of D_4 remains unclear, as we cannot identify any potential scattering vector from the ARPES data that would quantitatively fit the periodicities observed in the QPI experiments.

More detailed information about the dispersion of the surface bands within the full k-plane is obtained from the constant energy cuts in figures 6(c) and (d) that depict the photoemission intensity as a function of both wave vector components k_x and k_y parallel to the surface at fixed energy. In figure 6(c) one can discern two inner contours that correspond to the split s, p_z-band. Note that the contour originating from the branches l2 and r2 shows a hexagonal deformation. The cusps of the hexagonal contour point along the $\overline{\Gamma K}$ direction, implying $m^*_{\overline{\Gamma K}} > m^*_{\overline{\Gamma M}}$ for the branches l2 and r2. The contour corresponding to the p_x, p_y-band (branches l3 and r3) is best visible in figure 6(d). Also in this case we find a significant hexagonal warping with cusps of the contour pointing along the $\overline{\Gamma M}$ direction. Hence, for the p_x, p_y-band one has $m^*_{\overline{\Gamma M}} > m^*_{\overline{\Gamma K}}$.

Obviously, ARPES finds anisotropies of the s, p_z- and the p_x, p_y-band which are rotated by 30° with respect to each other. This finding is in line with our STM results and DFT calculations [7]. Qualitatively, the same situation has also been found for other isostructural surface alloys, such as Bi/Cu(111) [12, 13], Sb/Cu(111) [12] and Sb/Ag(111) [10]. Within a tight-binding picture we can interpret the rotated anisotropy of the two bands by assuming that a smaller effective mass corresponds to a larger orbital overlap. For the p_x, p_y-band the orbital overlap is then maximal along the direction connecting two neighbouring Pb atoms ($[1\bar{1}0]$ corresponding to $\overline{\Gamma K}$). On the other hand, in the case of the s, p_z-band the orbital overlap is largest along the direction connecting a Pb atom with its neighbouring Ag atoms ($[11\bar{2}]$ corresponding to $\overline{\Gamma M}$).

Hence, for the p_x, p_y-band and the s, p_z-band the lateral atomic bonding appears to be dominated by Pb–Pb and Pb–Ag nearest neighbour interaction, respectively.

With all parameters being determined we can exclude the band model schematically represented in figure 1(b). Instead, our data are consistent with the smaller relaxation model sketched in figure 1(c), where no hybridization between the two Rashba bands takes part.

3.2. Theoretical results: DFT

In figure 7(a) we show the calculated spin-resolved band structure of the Pb-derived states around the Fermi level (E_F) for a Pb relaxation of $\Delta_z = 0.67$Å. It is clearly seen that the s, p_z states with a band onset at about 0.5 eV show a strong Rashba-type spin polarization (as well as the p_z states at 2.5 eV), while the $m_{1/2}$-bands, the band onset of which is at 1.5 eV, exhibit a more complex spin texture. In particular around the $\bar{\Gamma}$-point the polarization decreases rapidly and even exhibits a reversal of the spin direction at some **k**-points . As the $m_{1/2}$-bands show no direct crossing with the s, p_z-bands (in contrast to the $BiAg_2$ case and the $PbAg_2$ with stronger relaxation), for larger k-values the spin direction reverses again and increases to larger momentum values.

To shed light on the origin of this loss of spin polarization near the $\bar{\Gamma}$-point, we show the spin- and orbital-resolved band structure in figure 7(b) focusing on the p_x and p_y states. Apparently, near the Brillouin-zone the states consist of a mixture of p_x with one spin-orientation and p_y states of the opposite spin orientation. It is well known from hole-states in semiconductors that spin–orbit coupling at small momenta can lead to the formation of orbital-moment-carrying states ($m_j = 1/2$) [23], while Rashba-type spin–orbit coupling dominates at larger k–values and forces the spin direction in-plane. Additionally, crystal-field effects decouple the p_x and p_y states according to the momentum direction.

Although an apparent decrease of spin polarization for the $m_{1/2}$ states at small k-values is clearly visible in figure 7, we cannot directly identify the origin of this reduction. In principle, also an increased out-of-plane component of the spin moment may lead to the same behavior. We checked for this possibility and found no significant spin component along the surface normal, but rather a mixture of strongly in-plane polarized p_x and p_y orbitals with opposite spin polarization. We have to note here that, although the total spin polarization is dramatically reduced near the center of the Brillouin-zone, the scattering from **k** to $-$**k**, i.e. between time-reversal partners, is still prohibited by time reversal symmetry [24].

Finally, we can turn to the question why the intra-band scattering—as indicated by the arrow in figure 7(b)—is allowed, despite the fact that initial and final states are dominantly of opposite spin character. Since the total momentum, **J**, has to be conserved in the scattering process, the associated transfer of spin angular momentum has to be compensated by an equivalent transfer of orbital momentum, **L**. Loosely speaking we can say that, if $\Delta\mathbf{J} = \Delta\mathbf{L} + 1/2\Delta\mathbf{S} = 0$, a 180° reversal of spin **S** needs to be compensated by a 90° rotation

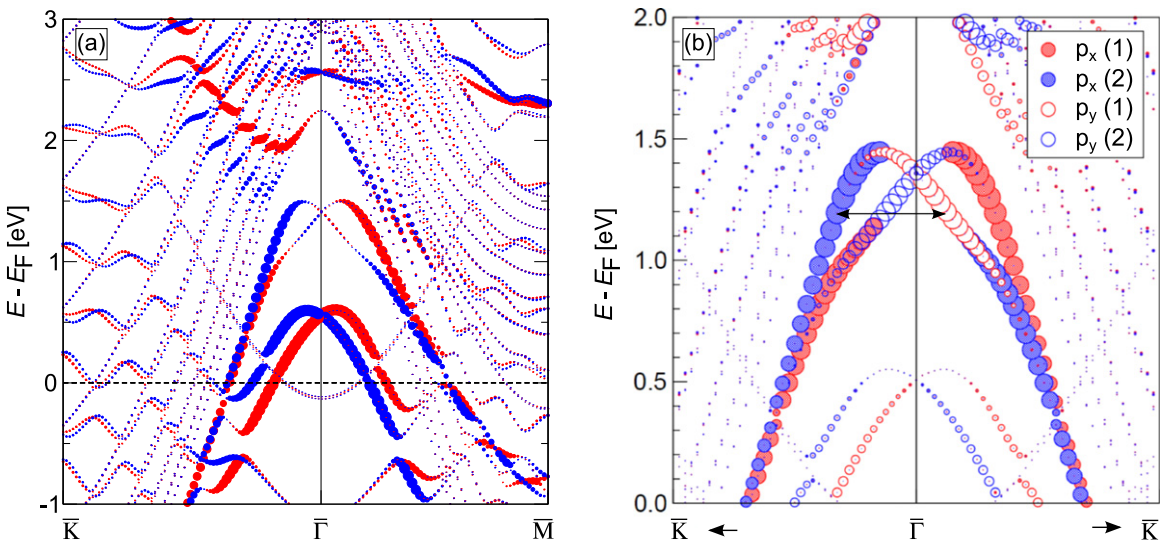

Figure 7. (a) Calculated band structure of the $PbAg_2$ layer on a nine-layer Ag(111) film. The Pb relaxation is fixed at $\Delta_z = 0.67$ Å. Red and blue colors indicate the spin polarization with respect to a spin-quantization axis that is perpendicular to the **k**-vector and surface normal. (b) Spin- and orbital-resolved band structure of the $PbAg_2$ surface alloy. Open and full circles show contributions from p_x and p_y orbitals, respectively. The size of the symbols in (a) and (b) indicates the degree of spin polarization.

of the orbital moment, i.e. from a p_x to a p_y orbital or vice versa. This is exactly the process allowed by the spin-flip (off-diagonal) part of the spin–orbit coupling[6] [25].

Indeed, the scattering process indicated by the black arrow in figure 7(b) connects p_x to p_y orbitals of opposite spin and is, therefore, allowed. A forward scattering process, as could be imagined in the $PbAg_2$ surface alloy between different bands of the same spin, can be excluded since it involves scattering from a p_x to a p_y orbital without a spin-flip. The interpretation of scattering events in terms of spin polarization of the involved bands cannot be drawn from a plot of the spin polarization of the states (like figure 7(a)) alone, since it is not directly possible to draw conclusions about allowed or forbidden quasi-particle scattering events. Only in a simple case, i.e. when the involved states do not carry orbital moments (s, p_z, d_{z^2}), the Rashba picture of spin polarization holds and selection rules can be directly inferred. In the case of the Bi(110) surface analyzed in this way [26] this was meaningful, since the surface states of this surface are of p_z character. In the present system, however, such assignments are misleading, since—in addition to the spin—also the orbital character has to be taken into account. In the same spirit the STM data of [17] can be reconciled with the calculations presented in [7], as we checked by explicit calculations.

[6] The spin–orbit coupling Hamiltonian can be written as $H_{\mathrm{SOC}} = \xi \mathbf{l} \cdot \mathbf{s} = \xi l_z s_z + \frac{\xi}{2}(l^+ s^- + l^- s^+)$, whereas the spin-flip part is represented by the second term containing the ladder operators $l^{+/-} s^{-/+}$.

4. Summary

In summary we were able to characterize two Rashba-split surface states in $(\sqrt{3} \times \sqrt{3})$ Pb/Ag (111)$R30°$. Tunneling spectroscopy shows two characteristically shaped peaks in the empty DOS. These peaks are fit by thermally broadened van-Hove-like singularity and identified as signatures of Rashba-split bands. The combination of ARPES and QPI mapping not only allows the reconstruction of the band structure of Pb/Ag(111) in the occupied and empty states but also makes the clear assignment of QPI scattering vectors possible. It is shown that both intra- and inter-band scattering events occur. DFT calculations reveal that in order to evaluate the interference pattern of QPI maps besides the spin also the orbital momentum of the involved electronic states has to be considered. Namely, spin-flip scattering events may be allowed as long as the total momentum **J** can be conserved if it is accompanied by a corresponding change of angular momentum.

Acknowledgments

This work has been funded by FOR1162 (projects P3 and P5). The publication was funded by the German Research Foundation (DFG) and the University of Wuerzburg in the funding programme Open Access Publishing. We acknowledge valuable discussion with D Wegner (Universität Münster). GB acknowledges supercomputing resources from the Jülich Supercomputing Centre (JSC) and insightful discussions with A Mugarza.

References

[1] Dresselhaus G 1955 *Phys. Rev.* **100** 580–6
[2] Bychkov Y A and Rashba E I 1984 *J. Phys. C: Solid State Phys.* **17** 6039
[3] LaShell S, McDougall B A and Jensen E 1996 *Phys. Rev. Lett.* **77** 3419–22
[4] Pacilé D, Ast C R, Papagno M, Da Silva C, Moreschini L, Falub M, Seitsonen A P and Grioni M 2006 *Phys. Rev.* B **73** 245429
[5] Ast C R, Wittich G, Wahl P, Vogelgesang R, Pacilé D, Falub M C, Moreschini L, Papagno M, Grioni M and Kern K 2007 *Phys. Rev.* B **75** 201401
[6] Ast C R, Henk J, Ernst A, Moreschini L, Falub M C, Pacilé D, Bruno P, Kern K and Grioni M 2007 *Phys. Rev. Lett.* **98** 186807
[7] Bihlmayer G, Blügel S and Chulkov E V 2007 *Phys. Rev.* B **75** 195414
[8] Premper J, Trautmann M, Henk J and Bruno P 2007 *Phys. Rev.* B **76** 073310
[9] Meier F, Dil H, Lobo-Checa J, Patthey L and Osterwalder J 2008 *Phys. Rev.* B **77** 165431
[10] Moreschini L *et al* 2009 *Phys. Rev.* B **79** 075424
[11] Mirhosseini H, Henk J, Ernst A, Ostanin S, Chiang C T, Yu P, Winkelmann A and Kirschner J 2009 *Phys. Rev.* B **79** 245428
[12] Moreschini L, Bendounan A, Bentmann H, Assig M, Kern K, Reinert F, Henk J, Ast C R and Grioni M 2009 *Phys. Rev.* B **80** 035438
[13] Bentmann H, Forster F, Bihlmayer G, Chulkov E V, Moreschini L, Grioni M and Reinert F 2009 *Europhys. Lett.* **87** 37003
[14] Gierz I, Meier F, Dil J H, Kern K and Ast C R 2011 *Phys. Rev.* B **83** 195122
[15] Hirayama H, Aoki Y and Kato C 2011 *Phys. Rev. Lett.* **107** 027204

[16] Bentmann H, Abdelouahed S, Mulazzi M, Henk J and Reinert F 2012 *Phys. Rev. Lett.* **108** 196801
[17] El-Kareh L, Sessi P, Bathon T and Bode M 2013 *Phys. Rev. Lett.* **110** 176803
[18] Steinbrecher M, Harutyunyan H, Ast C R and Wegner D 2013 *Phys. Rev.* B **87** 245436
[19] Dalmas J, Oughaddou H, Léandri C, Gay J M, Le Lay G, Tréglia G, Aufray B, Bunk O and Johnson R L 2005 *Phys. Rev.* B **72** 155424
[20] Hirahara T, Komorida T, Sato A, Bihlmayer G, Chulkov E V, He K, Matsuda I and Hasegawa S 2008 *Phys. Rev.* B **78** 035408
[21] Gierz I, Stadtmüller B, Vuorinen J, Lindroos M, Meier F, Dil J H, Kern K and Ast C R 2010 *Phys. Rev.* B **81** 245430
[22] Müller U, Carnal D, Siegenthaler H, Schmidt E, Lorenz W J, Obretenov W, Schmidt U, Staikov G and Budevski E 1992 *Phys. Rev.* B **46** 12899–901
[23] Winkler R 2005 *Phys. Rev.* B **71** 113307
[24] Qi X L and Zhang S 2010 *Phys. Today* **63** 33
[25] Zhang H, Freimuth F, Bihlmayer G, Ležaić M, Blügel S and Mokrousov Y 2013 *Phys. Rev.* B **87** 205132
[26] Pascual J I *et al* 2004 *Phys. Rev. Lett.* **93** 196802